Interval-based Uncertainty Bounding for Terrestrial Laser Scanning Observations

Reza Naeimaei[1,*], Steffen Schön[2]

[1,2] Institut für Erdmessung (IfE), Leibniz University Hannover, Hannover, Germany
(naeimaei@ife.uni-hannover.de, schoen@ife.uni-hannover.de)

Keywords: Interval arithmetic, Terrestrial Laser Scanners, Observation Uncertainty.

Abstract

One of the main fields of engineering geodesy is deformation monitoring of natural and man-made structures. Infrastructure objects such as bridges, dams, and tunnels are of special interest because their operational safety must be ensured at all times. Area-based deformation analysis can be effectively conducted using terrestrial laser scanners (TLS). Unlike the limited, pre-selected, and point-based measurements used in traditional approaches, TLS samples the environment with millions of points without the need to signal the points. Point clouds data from TLS are influenced by remaining systematic errors as well as random noise. These sources of uncertainty are frequently handled using probabilistic approaches, which may provide an inadequate or overoptimistic representation of the overall uncertainty in point cloud data. In this contribution, an alternative approach based on interval mathematics is proposed to bound the uncertainty due to remaining systematic errors. To this end, a sensitivity analysis of TLS observation correction models is performed, and typical variability of the input parameters, such as temperature, pressure, humidity, and temperature gradients, as well as instrument misalignment, is assessed. Subsequently, error bands for the polar measurement elements in the form of intervals are obtained. While variance propagation follows a quadratic form, interval-based techniques enable linear uncertainty propagation, which is more effective for describing residual systematic uncertainty and worst-case scenarios. The methodology will be explained in detail, and typical values for the obtained intervals will be discussed and highlighted in a simulation study.

1. Introduction

Terrestrial Laser Scanners (TLS) are widely utilized for deformation monitoring in both natural environments and built infrastructure. They play a vital role in assessing structural conditions and informing decision-making throughout the construction, operational, and maintenance phases. Ensuring structural integrity at all times is of paramount importance, as undetected damage can lead to severe human and financial consequences (Shen et al., 2023). Therefore, accurate and reliable deformation monitoring is essential to prevent serious failures. A key challenge in ensuring monitoring accuracy is understanding how well the uncertainty of deformation is represented and how this uncertainty can be safely bounded. In this context, the development of an effective uncertainty budget is crucial. This includes not only the random variability of observations (stochastic errors) but also the second component, systematic errors that may persist (Schön and Kutterer, 2006).

In TLS applications, it is critical to account for all types of errors, both systematic and random, that inevitably affect measurements. Such errors can originate from various sources, including instrument misalignment, atmospheric conditions, scan geometry, object surface properties, as well as registration issues (Soudarissanane et al., 2011). Although some of these errors can be reduced or mitigated using correction models, calibration techniques, or carefully designed measurement strategies, it is important to recognize that such methods do not completely eliminate all error sources. Systematic effects and random variability will always persist and must be considered as part of the overall uncertainty in TLS measurements. The following factors highlight why systematic influences remain and random variations continue to occur:

- Calibration parameters may not accurately describe misalignment.
- There is insufficient knowledge about the range of influence of atmospheric parameters due to their unpredictable behavior.
- There may be insufficient data to accurately model errors related to scanning geometry, and stochastic propagation might not always be adequate.
- The interaction between the laser beam and the surface can be unpredictable, as there is no general rule for how laser light interacts with different surfaces.
- Measurements are often pre-processed with unknown functions.
- Manufacturers may not provide all relevant information to users.

All these uncertainty components in measurements (range (r), horizontal angle (φ), and vertical angle (θ)) are typically treated as part of the stochastic error. A quadratic error propagation is then applied to transfer these uncertainties to the target parameters. Under the assumption of a normal distribution for observation errors, common measures of stochastic uncertainty in the positional domain include confidence regions like point confidence ellipsoids (BIPM et al., n.d.). However, the exact error distribution is typically unknown, and exclusively depending on probabilistic modeling to account for remaining systematic errors may not be sufficient. Therefore, alternative methods for uncertainty bounds and propagation should be explored.

Interval analysis was first developed in mathematics to deal with rounding errors and their spread in scientific calculations (Herzberger and Alefeld, 1983). Its applications have since expanded into robotics and robust localization, with early developments rooted in control theory, particularly in the work of (Jaulin et al., 2001). Guyonneau et al. (2014) proposed an

Interval Analysis Localization algorithm utilizing Light Detection and Ranging (LiDAR) and odometry data, demonstrating improvements over Monte Carlo Localization. By relying on LiDAR, odometry, and a discrete map of an indoor environment, their approach enables a robot to determine its position and orientation within the map without prior knowledge of its initial location. Voges and Wagner (2021) introduced an interval-based method to fuse data from cameras and LiDAR systems in a guaranteed manner, showing how measurement and calibration uncertainties can be propagated to features used in robot localization. Further extending these concepts, Ehambram et al. (2022) presented an interval-based visual-inertial LiDAR SLAM approach, which propagates bounded sensor errors using interval analysis and is stabilized through poses anchored by Global Navigation Satellite Systems (GNSS) and Inertial Navigation Systems (INS) data, outperforming classical SLAM graph optimization in uncertainty estimation. Le Bars et al. (2022) implemented an interval-based INS for orientation and position estimation, highlighting its resilience to outliers and its capacity for rapid, reliable control. This method has also been employed to validate robust navigation protocols for an autonomous boat.

In the field of geodesy, interval analysis was introduced by Reinhart (1975) and Schmitt (1977), who proposed the min-max method to handle tolerances. Kutterer (1994) advanced this approach by investigating the interval-based least-squares estimator and extending interval descriptions within the broader framework of fuzzy sets and observation imprecision, as discussed by Möller and Beer (2013). Later, Schön (2003) explored the optimization of deformation networks under interval uncertainty. Recently, Su and Schön (2021, 2022) refined the derivation of observation intervals for GNSS, specifically considering tropospheric and ionospheric refraction, as well as multi-path effects. Using extensive real-world data from both independent experiments and permanent GNSS reference stations, the derived observation intervals were successfully validated, demonstrating their ability to enclose parameter variations accurately.

Few studies have thoroughly investigated the determination of meaningful bounds for observation intervals, particularly in the context of TLS applications. Much of the existing literature on uncertainty bounds - particularly those derived from interval analysis - has focused on localization in robotics and navigation systems such as GNSS, with limited attention to TLS. To bridge this gap, we propose an interval-based approach for determining uncertainty bounds in TLS measurements that incorporates residual systematic effects, while random variations are assumed to follow a normal distribution. This method offers a more robust framework for uncertainty management in TLS. This advancement is crucial for accurate area-based deformation analysis.

The structure of the rest of this paper is outlined below: Sec. 2 reviews the basics of interval analysis, including how intervals can be used in sensitivity analysis and uncertainty propagation. Sec. 3 presents the measurement model for TLS applications and describes the correction model for instrument and atmospheric error sources. Sec. 4 presents the experimental results for sensitivity analysis of the two error sources and compares the stochastic and interval-based uncertainty propagation for simulated observations. Finally, concluding remarks and an outlook are provided in Sec. 5.

2. Methodology

The following section provides a brief introduction to interval analysis, based on the work of Jaulin et al. (2001). Next, it reviews the concept of sensitivity analysis in the context of interval analysis. Finally, it explains the concept of uncertainty propagation using interval analysis.

2.1 Basics of interval analysis

Interval analysis is a branch of set theory that extends real arithmetic operations in $\mathbb{R}$ to intervals in $\mathbb{IR}$. An interval $[a]$ is defined by its lower bound $\underline{a}$ and upper bound $\overline{a}$, such that:

$$[a] = [\underline{a}, \overline{a}] = \{a \in \mathbb{R} \mid \underline{a} \leq a \leq \overline{a}\}. \tag{1}$$

Both the lower and upper bounds can be infinite. Equation 2 represents the radius $rad([a])$ and the midpoint $mid([a])$ for any bounded, non-empty interval $[a]$.

$$rad([a]) = \frac{\overline{a} - \underline{a}}{2} \quad , \quad mid([a]) = \frac{\overline{a} + \underline{a}}{2} \tag{2}$$

Most real-valued arithmetic operations can be extended to intervals, including the basic operations $+$, $-$, $\times$, $\div$, $\cup$, $\cap$, as well as functions such as $\sin$, $\cos$, $\exp$. These operations are defined as:

$$[a] \lozenge [b] = \{a \lozenge b \in \mathbb{R} \mid a \in [a], b \in [b]\} \tag{3}$$

where $[a]$ and $[b]$ are intervals, and $\lozenge$ represents any of the aforementioned algebraic operations. Readers seeking a deeper background in interval analysis may refer to works such as Jaulin et al. (2001) and Moore et al. (2009).

2.2 Sensitivity analysis

Here, sensitivity analysis examines how slight variations in a model's input parameters influence its output (BIPM et al., n.d.). This approach aids in identifying the impact of each input on the system's behavior and supports the estimation of systematic error bounds alongside random uncertainties.

Let $f(\mathbf{s})$ represent a specific model with n independent input parameters, where $\mathbf{s} = s_i, i = 1, \ldots, n$. Sensitivity analysis is conducted using the total differential of f, evaluated at predefined parameter values $\mathbf{s}^*$.

$$df = \sum_{i=1}^{n} \frac{\partial f(\mathbf{s}^*)}{\partial s_i} ds_i = \mathbf{F} \cdot \mathbf{ds}, \tag{4}$$

Here, $\mathbf{F}$ represents a $1 \times n$ matrix containing the partial derivatives of the function f with respect to the influence parameters, and $\mathbf{ds}$ reflects the associated uncertainties or variations in these parameters.

2.3 Propagating uncertainty

Equation 4 gives rise to various approaches for handling and propagating uncertainty: If we consider the variance $\sigma_{s_i}^2$ as the measure of uncertainty for the influence parameters, we obtain the classical law of quadratic variance propagation as follows:

$$\sigma_f^2 = \sum_{i=1}^{n} \left[\frac{\partial f(\mathbf{s}^*)}{\partial s_i} \right]^2 \sigma_{s_i}^2 \tag{5}$$

In traditional methods, all sources of uncertainty are modeled using stochastic techniques; however, to achieve a more accurate uncertainty estimate, remaining systematic errors must also be taken into account. Kutterer Kutterer (1999) proposed a sensitivity analysis technique based on interval mathematics to incorporate remaining systematic errors via interval modeling. This methodology was subsequently employed in geodetic monitoring networks (Schön and Kutterer, 2005b) and GPS data analysis (Schön and Kutterer, 2005a; Dbouk, 2021; Su and Schön, 2022).

If the remaining uncertainty for each influence parameter s_i is bounded within the range $s^*i \pm \Delta s_i$, with Δ_{s_i} defining the interval radius, then the output uncertainty of the model is constrained by the corresponding interval radius Δ_f:

$$\Delta_f = \sum_{i=1}^{n} \left| \frac{\partial f(\mathbf{s}^*)}{\partial s_i} \right| \Delta_{s_i} = |\mathbf{F}| \cdot \mathbf{\Delta_s} \tag{6}$$

In Equation 6, due to the computation rules in interval mathematics, the absolute values of the partial derivatives have to be used. Consequently, interval uncertainties in the inputs propagate linearly to the model output, yielding $f + [-\Delta_f, \Delta_f]$, where $f = f(\mathbf{s}^*)$ reflects the effect of parameter variation.

In a similar manner, the analysis is applied to the TLS point cloud $\mathbf{x} = g(\mathbf{l})$. Assuming that the variance-covariance matrix (VCM) of the observations ($\mathbf{l}$), denoted as $\Sigma_\mathbf{l}$, is known, uncertainties are propagated using $\mathbf{G}$ as the partial derivatives matrix with respect to observations. The covariance matrix of the points $\Sigma_\mathbf{x}$ is then computed as:

$$\Sigma_x = \mathbf{G} \cdot \Sigma_l \cdot \mathbf{G}^T \tag{7}$$

This propagation allows for the definition of a confidence region corresponding to a given confidence level α, i.e. an ellipsoid in 3D space or an ellipse in 2D space, respectively, representing the stochastic (i.e., random) variability of the point positions.

However, to present realistic uncertainty, an alternative approach is needed to account for the remaining systematic error in addition to the random variability. To assess the uncertainty due to remaining systematic effects, Kutterer (1994) proposed a straightforward method for propagating uncertainty based on intervals:

$$\Delta_x = |\mathbf{G}| \cdot \Delta_l \tag{8}$$

Here, Δ_l represents the interval radii of all observations, computed based on sensitivity analysis, and $|\mathbf{G}|$ represents the absolute values of the partial derivatives that linearly propagate the uncertainty to the position domain.

The point position $\mathbf{x}$ along with the interval radius Δ_x defines an error box surrounding the point in the positional domain, whose edges are aligned with the axes of the coordinate system used to specify the point location, as illustrated later. However, the feasible region of position variation is initially characterized at first order by a zonotope (Schön and Kutterer, 2005a).

$$\mathcal{Z} := \{\mathbf{x}_i \in \mathbb{R}^3 \;\; \mathbf{x}_i = \mathbf{x} + \sum_{i=1}^{p} \beta_i \mathbf{g}^{(i)} \Delta_{l_i}, \; \beta_i \in [-1, 1] \text{ for } i = 1, \ldots, p\} \tag{9}$$

Here, $\mathbf{g}^{(i)}$ denotes the i-th column vector of the matrix $\mathbf{G}$. The resulting zonotope is centered at the position $\mathbf{x}$ and generated by the vectors $\mathbf{g}^{(i)}$, each scaled by the corresponding observation's interval radius Δ_{l_i}. The interval box represents the smallest axis-aligned enclosure that contains the zonotope within the given coordinate system of the feasible point position. A zonotope is a convex polytope that is symmetric with respect to its center and can be interpreted as the Minkowski sum of a finite set of line segments (Ziegler, 1995). Zonotopes and interval boxes will be employed to assess how remaining systematic errors in the observations influence the estimated parameters.

3. Measurement model for TLS application

The next section outlines the geometric configuration of a typical TLS system and then discusses the correction models addressing both instrumental and atmospheric error sources.

3.1 TLS measurement geometry

In many cases, Cartesian coordinates are not directly measured but derived from related quantities through a measurement model. In TLS, these coordinates are computed by converting spherical coordinates (r, φ, θ) into Cartesian coordinates (x, y, z) (figure 1). The Cartesian coordinates of the i^{th} point

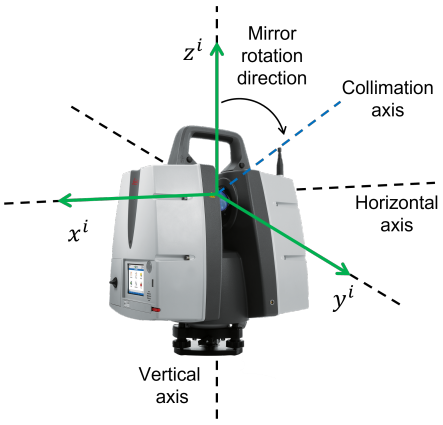

Figure 1. Coordinate system of a TLS as an example in the Leica ScanStation P50 with respect to the main instrument axes (Leica GmbH, 2017).

in the scanner system are determined using the following equations:

$$\begin{bmatrix} x_i \\ y_i \\ z_i \end{bmatrix} = \begin{bmatrix} r_i \sin(\theta_i) \sin(\varphi_i) \\ r_i \sin(\theta_i) \cos(\varphi_i) \\ r_i \cos(\theta_i) \end{bmatrix} \tag{10}$$

The observed values of r, φ, and θ may contain errors that must be accounted for. These errors arise from various sources, including atmospheric conditions and instrument misalignment, both of which are critical for accurate point cloud data.

Instrumental misalignments introduce systematic errors in the range and angular measurements, while atmospheric effects primarily affect the range and vertical angle measurements. To account for these errors, corrections for instrument misalignment $(C_r^{ins}, C_\varphi^{ins}, C_\theta^{ins})$ and atmospheric effects $(C_r^{atm}, C_\theta^{atm})$ are applied to the i^{th} observations. As a result, the corrected observations $(r^c, \varphi^c, \theta^c)$ are obtained.

$$r_i^c = r_i + C_{r_i}^{ins} + C_{r_i}^{atm} \tag{11}$$

$$\varphi_i^c = \varphi_i + C_{\varphi_i}^{ins} \tag{12}$$

$$\theta_i^c = \theta_i + C_{\theta_i}^{ins} + C_{\theta_i}^{atm} \tag{13}$$

3.2 Instrument correction model

In this study, a comprehensive geometric error model developed by the National Institute of Standards and Technology (NIST) is adopted. This particular model is designed to account for various error sources, including offsets, tilts, and eccentricities in the optomechanical components of TLS (Muralikrishnan et al., 2015). Given the high precision of the scanners examined, errors related to the angular encoders can be neglected. Consequently, a simplified version of the NIST model, comprising ten parameters as detailed in Table 1, is employed to effectively calibrate these high-end scanners (Medić et al., 2019). The correction model applied to range and angular measurements can be formulated as follows:

$$C_{r_i}^{ins} = x_2 \sin(\theta_i) + x_{10} \tag{14}$$

$$C_{\varphi i}^{ins} = \frac{x_{1z}}{r_i \tan(\theta_i)} + \frac{x_3}{r_i \sin(\theta_i)} + \frac{(x_{5z} - x_7)}{\tan(\theta_i)} + \frac{2x_6}{\sin(\theta_i)} + \frac{x_{1n}}{r_i} \tag{15}$$

$$C_{\theta_i}^{ins} = \frac{(x_{1n} + x_2)\cos(\theta_i)}{r_i} + x_4 + x_{5n}\cos(\theta_i) - \frac{x_{1z}\sin(\theta_i)}{r_i} - x_{5z}\sin(\theta_i) \tag{16}$$

Table 1. Calibration parameters of high-end TLS

Parameter	Description
x_{1n} $[mm]$	Horizontal beam offset
x_{1z} $[mm]$	Vertical beam offset
x_2 $[mm]$	Horizontal axis offset
x_3 $[mm]$	Mirror offset
x_{10} $[mm]$	Rangefinder offset
x_4 ["]	Vertical index offset
x_{5n} ["]	Horizontal beam tilt
x_{5z} ["]	Vertical beam tilt
x_6 ["]	Mirror tilt
x_7 ["]	Horizontal axis error (tilt)

3.3 Atmospheric correction model

As with electronic distance measurements (EDM) in total stations, TLS range measurements are notably affected by variations in air temperature and pressure, especially across long distances. The influence of partial water vapor pressure is disregarded due to its relatively minor impact. In this section, we describe the range correction model, with the ”First Velocity Correction” explained in (Rüeger, 2012). The atmospheric correction for range measurements can be expressed as:

$$C_{r_i}^{\text{atm}} = r_i(n_{\text{ref}} - n) \tag{17}$$

where n_{ref} is the reference refractive index, defined as the value at which the distance meter provides a direct and correct readout. The manufacturer establishes it by selecting a suitable unit length and adjusting the main oscillator to a modulation frequency that corresponds to an average refractive index typically encountered in the field. The variable n denotes the refractive index in the medium, which causes the speed of light in the atmosphere to be reduced compared to that in a vacuum.

The speed at which electromagnetic waves propagate is determined by the group refractive index, which varies with the wavelength λ_L.

According to the resolutions of the International Association of Geodesy (IAG), the group refractivity n_{g} of standard air—containing 0.0375% CO_2—should be computed under reference conditions of $T = 273.15$ K, air pressure $P = 1013.25$ hPa, and partial water vapor pressure $e = 0.0$ hPa as follows:

$$(n_{\text{g}} - 1) \cdot 10^6 = 287.6155 + 3\left(\frac{1.6288}{\lambda_L^2}\right) + 5\left(\frac{0.0136}{\lambda_L^4}\right) \tag{18}$$

To account for actual atmospheric conditions, the standard atmosphere must be corrected using the following equation (Rüeger, 2012):

$$(n - 1) = (n_{\text{g}} - 1)\left(\frac{273.15\ P}{1013.25\ T}\right) - \left(\frac{11.27\ e}{T}\right)10^{-6} \tag{19}$$

In this equation, n_g is the reduced group refractivity from the standard atmosphere to the current atmospheric conditions, n_l is the group refractive index under the current atmosphere.

Beyond its impact on distance measurements, atmospheric refraction also alters vertical angle observations. This phenomenon may result in image scintillation, especially under conditions with strong vertical temperature gradients near the surface (Brunner, 1984). Various formulations exist for vertical angle corrections; however, the current formulation is based on the derivable equation proposed by (Kharaghani, 1987):

$$C_{\theta_i}^{\text{atm}} = \frac{r_i}{2E_R} \cdot k \tag{20}$$

where r_i is the measured range, E_R is the Earth’s mean radius (6381 km), and k is the refraction coefficient, accounting for the curved light path (Kharaghani, 1987). The Gaussian constant $k = +0.13$ is commonly used by default (Brunner, 1984), though it varies throughout the day and depends on the temperature gradient $\frac{\partial T}{\partial z}$ in K/m (Kharaghani, 1987).

When focusing on a specific region, the local refraction coefficient k_{loc} can be defined as a function of temperature T, pressure P, and the vertical temperature gradient (VGT) in that region (Kharaghani, 1987):

$$k_{loc} = 502.7 \cdot \frac{p}{T^2}\left(0.0343 + \frac{\partial T}{\partial z}\right) \tag{21}$$

4. Experimental result

The following section presents a sensitivity analysis for all influence parameters related to instrumental and atmospheric sources. Subsequently, it illustrates the results of uncertainty propagation in terms of intervals and compares them with the classical approach.

4.1 Sensitivity analysis experiments

Based on the definition provided in the introduction, the remaining systematic error can be described as a worst-case scenario. In this context, the maximum variation in calibration parameters represents the worst-case scenario.

To address this, for instrument error sources, we rely on the results of Medić et al. (2019), who performed four repeated calibrations for the Leica ScanStation P50. Table 2 presents the calibration parameters from these four repetitions, and the absolute maximum difference between the parameters is used as the deviation in the sensitivity analysis.

Table 2. Leica ScanStation P50 calibration results for 4 repeated calibrations (Medić et al., 2019).

Par.	$\hat{x}_1$	$\hat{x}_2$	$\hat{x}_3$	$\hat{x}_4$	$\hat{x}_{\lvert max-min \rvert}$
x_{1n} $[mm]$	0.07	0.08	0.05	0.01	0.07
x_{1z} $[mm]$	0.08	0.31	0.21	0.14	0.23
x_2 $[mm]$	-0.12	-0.11	-0.12	-0.14	0.03
x_3 $[mm]$	-0.02	0.00	-0.06	-0.03	0.06
x_{10} $[mm]$	-0.16	0.03	0.01	-0.03	0.19
x_4 [”]	4.20	5.10	5.17	4.51	0.97
x_{5n} [”]	4.50	4.67	5.62	5.38	1.12
x_{5z} [”]	-12.00	-14.71	-14.33	-16.78	4.78
x_6 [”]	4.19	3.59	4.11	3.41	0.78
x_7 [”]	-22.35	-25.38	-26.31	-33.50	11.15

To ensure that the interval radius, computed by the absolute maximum difference ($\hat{x}_{|max-min|}$), can sufficiently overbound all possible remaining systematic errors, corrections are calculated both for the mean of all repetitions ($C^{ins}_{\hat{x}_{mean}}$) and for each individual repetition ($C^{ins}_{\hat{x}_i}$):

$$\left| C^{ins}_{\hat{x}_i} - C^{ins}_{\hat{x}_{mean}} \right| \leq \Delta^{ins}_{\hat{x}_{|max-min|}} \quad , \quad i = \{1, 2, 3, 4\} \quad (22)$$

Equation 22 holds true for each individual repetition, confirming that the interval radius adequately overbounds all possible remaining systematic errors.

Additionally, for the atmospheric conditions, the maximum difference in atmospheric parameters during the measurement campaign at the Brucher water dam in Germany is considered as the deviation for the sensitivity analysis. The values are given in Table 3. According to the technical specifications, air temperature is measured with an accuracy of $\pm 0.1^{\circ}C$ within the range of -25 $^{\circ}C$ to +70 $^{\circ}C$, air pressure with an accuracy of ± 1.5 hPa in the range of 750 hPa to 1100 hPa, and air humidity with an accuracy of ± 2.5 RH in the range of 11% to 90%. These measurements were obtained using a GFTB 200, a handheld meteorological sensor (Greisinger Electronic GmbH, 2013).

Table 3. absolute difference of atmospheric parameters

Par.	$\lvert max - min \rvert$
temperature $[^{\circ}C]$	14.9
pressure $[hPa]$	1.55
humidity $[hPa]$	6.07

With regard to VGT, there is no specific sensor to measure this parameter in the measurement campaign. Therefore, an empirical value for the uncertainty in an alpine region, provided by (Hennes, 2006), was used as a deviation in the sensitivity analysis. A standard deviation of 0.25 K/m in the lower atmosphere is given for alpine conditions. Figure 2 presents the sensitivity analysis results. For the instrumental aspects, sub-figures (a), (b), and (c) display the interval radii for range, horizontal angle, and vertical angle with respect to calibration parameters. The influence parameters show symmetric behavior before and after 180 degrees, so only the first half of the range is shown. In these sub-figures, the total interval radius

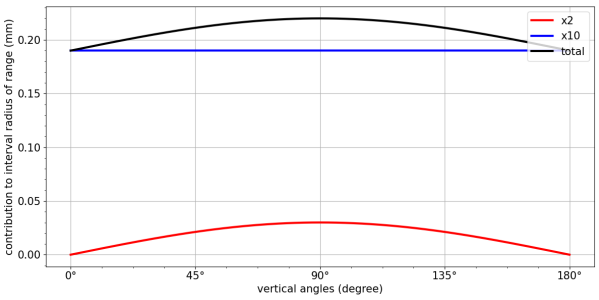

(a) Instrument part - Interval radius of range w.r.t. influence parameters

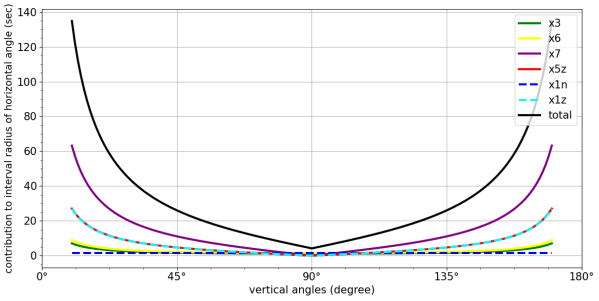

(b) Instrument part - Interval radius of horizontal angle w.r.t. influence parameters

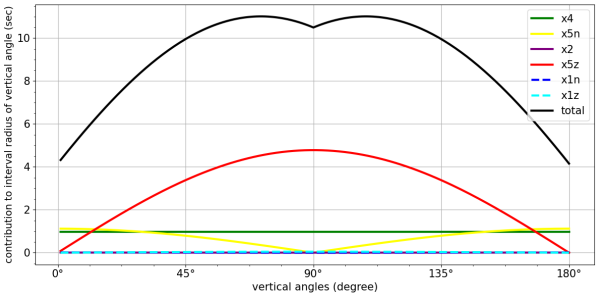

(c) Instrument part - Interval radius of vertical angle w.r.t. influence parameters

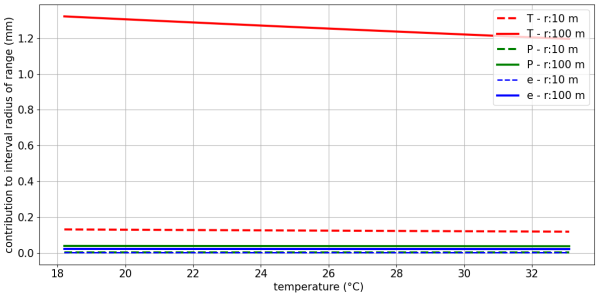

(d) Atmospheric part - Interval radius of range w.r.t. influence parameters

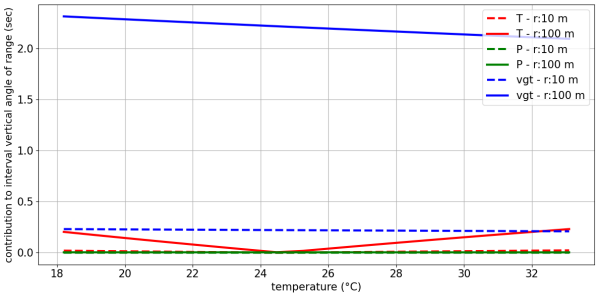

(e) Atmospheric part - Interval radius of vertical angle w.r.t. influence parameters

Figure 2. Interval radius of TLS observation due to instrument misalignment

(black line) peaks around a vertical angle of 90 degrees. For range, horizontal angle, and vertical angle, the parameters x_{10}, x_7 and x_{5z}, respectively, contribute the most to the interval radius. Similarly, sub-figures (d) and (e) illustrate the interval radii for range and vertical angle with respect to atmospheric parameters across different range measurements.

The figure demonstrates that the range can variate by up to 0.2 mm and 1.2 mm due to instrumental and atmospheric error sources, respectively. The vertical angle can variate by up to 140 arc seconds and 2.2 arc seconds due to instrumental and atmospheric error sources, respectively. Finally, the horizontal angle can variate by up to 11 arc seconds due to instrumental error sources.

4.2 Uncertainty propagation experiment

For the propagation of uncertainty in terms of intervals, we focus on simulations. By defining the origin and orientation of the local laser scanner coordinate system within the global reference frame, corresponding observations can be simulated. The simulation setup is illustrated in Figure 3, featuring the scanner positioned at coordinates $(10, 1, 1)$, while the lower-left corner of the plane is located at $(5, 5, 1)$. The plane measures 20 units in both width and height.

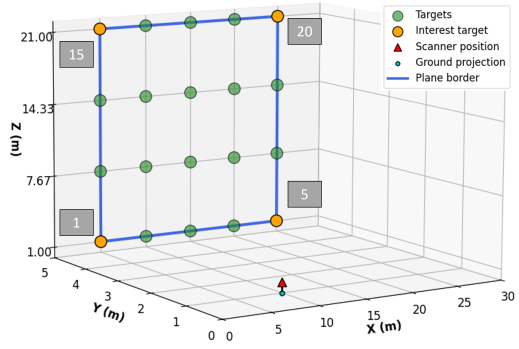

Figure 3. Simulation of plane and laser scanner observation

These simulated observations (l_s) are generated similarly to the real scanning process by increasing the vertical angle and horizontal direction. To achieve realistic results, systematic error (e_s) and random noise (e_r) are added to the simulated observations (l_s) as follows:

$$l = l_s + e_s + e_r \tag{23}$$

The inverse of the correction model for instrument error sources, computed using the mean values of all repeated calibration parameters listed in Table 2, is considered as the systematic error (e_s) and is given as follows:

$$e_s = -C^{ins}_{\hat{x}_{mean}} \tag{24}$$

The typical laser scanner error is represented by $\sigma_{r_i} = 1.2\,\text{mm} + r_i \cdot 0.01\,\text{mm/m}$ for range measurements, while angular errors are given as $\sigma_\phi = \sigma_\theta = 38.78\ \mu\text{rad}$ (Leica GmbH, 2017). These errors are utilized to compute zero-mean random noise that follows a normal distribution. Using the Monte Carlo method, random noise is generated multiple times (in this case, 2000 iterations) to illustrate the complete range of potential random variations, as follows:

$$e_r \sim \mathcal{N}(0, \sigma^2) \tag{25}$$

After simulating the TLS observations and incorporating both systematic and random errors, an instrument correction is applied. For this purpose, one of the four repetitions from Table 2 (in this case, the first column) is selected to compute the correction model, which is then applied to the observations.

Then, Cartesian coordinates based on these corrected observations are computed, and the true points, along with all noisy point samples, are represented from three different perspectives in Figure 4. A sensitivity analysis is subsequently conducted for the instrument correction models, followed by the computation of interval radii for all observations. The resulting uncertainty, based on the interval concepts explained in Section 2, is propagated and represented as an error box and a zonotope in the position domain, capturing the remaining systematic errors.

Figure 4 illustrates the uncertainty of four simulated points from different perspectives, visually distinguishing between remaining systematic errors and random variability. The dashed green line represents the line of sight of the observation, indicating the measurement direction from the scanner. The green point marks the true, noise-free point, while the light blue dots represent the noisy points after both systematic and random errors have been incorporated. Additionally, the blue point represents the mean of the light blue dots.

The distribution of noisy dots shows the random variability in the observations. In nearly all views, the dots are distributed along the ray direction, indicating that the uncertainty in range measurements is larger than in angular observations. Notably, range uncertainty is also dependent on the range itself, with uncertainty increasing at longer distances.

The red zonotope highlights the influence of the remaining systematic errors, visually representing how these uncertainties affect the position domain. The zonotope is oriented in the direction of observation; for instance, in the XY view, it is plotted along the range and horizontal angle. In contrast, the black dashed error box is aligned with the coordinate system and encloses the zonotope, providing a more conservative estimate of the total uncertainty, which includes systematic deviations.

5. Conclusion and Outlook

This paper presents an extended approach for addressing the two most significant types of uncertainty in TLS point clouds: stochasticity (random variations) and remaining systematic errors. Traditionally, these uncertainties are often treated using probabilistic methods, which can lead to inadequate or overly optimistic representations of the overall uncertainty in point cloud data. In many practical applications, it is essential to consider both random variability and systematic errors simultaneously. This work presents a new approach based on interval mathematics. This approach is used to bound uncertainties caused by remaining systematic errors. A sensitivity analysis was performed on the TLS observation correction models to assess the variability of influence parameters. Based on this analysis, error bounds in the form of intervals for the polar measurement elements were derived. Unlike variance propagation, which is quadratic in nature, the interval-based method provides a linear uncertainty propagation, making it better suited for characterizing remaining systematic uncertainties and their maximum possible impacts. This methodology has been explained in detail, and the typical values of the obtained intervals were derived and discussed, as well as illustrated through an experiment. The proposed method offers a

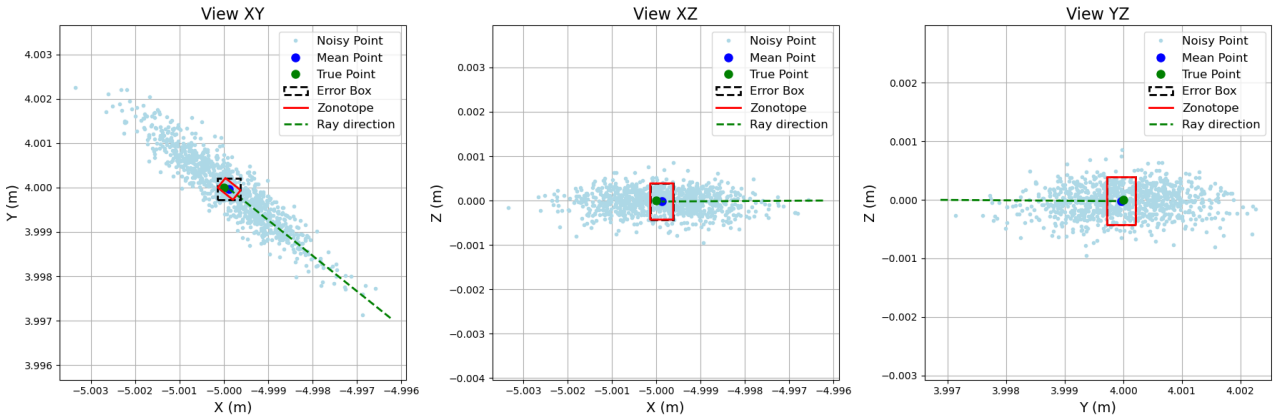

(a) 1st point

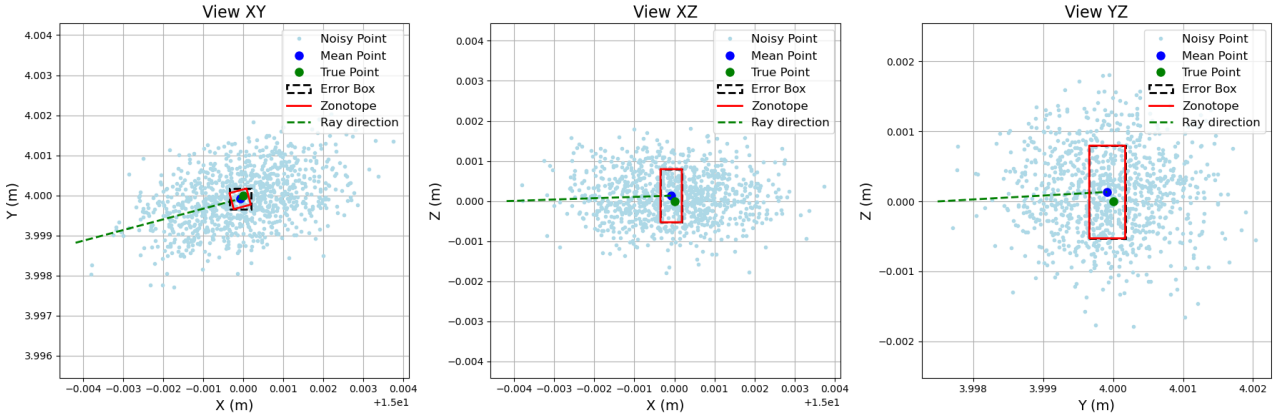

(b) 5th point

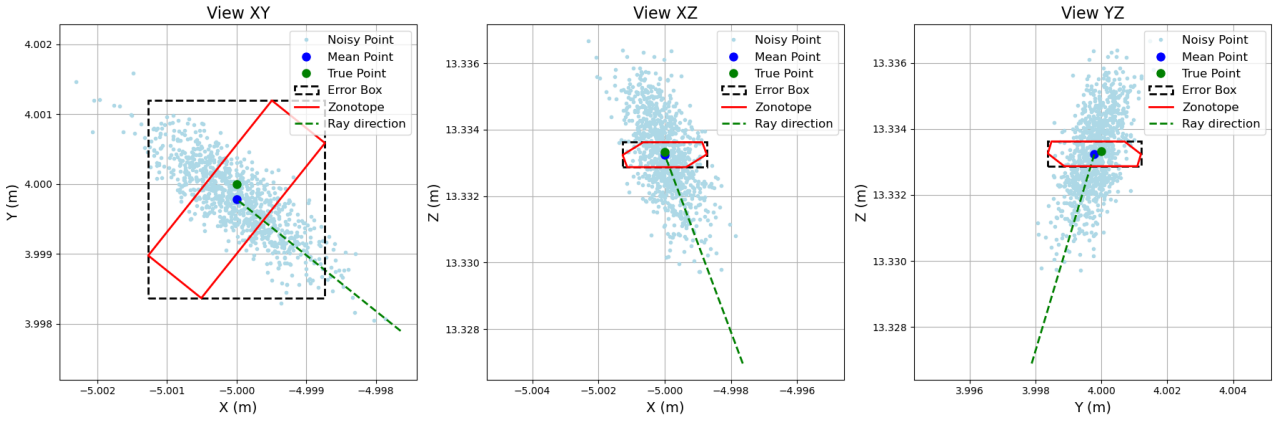

(c) 11th point

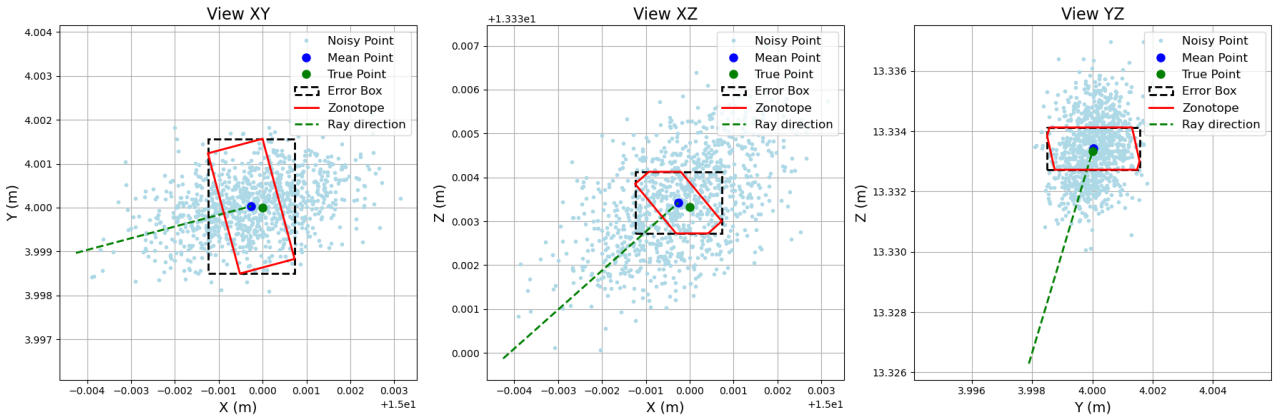

(d) 15th point

Figure 4. uncertainty representation in positional domain for four different points corresponding to Figure 3

This contribution has been peer-reviewed. The double-blind peer-review was conducted on the basis of the full paper.
https://doi.org/10.5194/isprs-annals-X-G-2025-599-2025 | © Author(s) 2025. CC BY 4.0 License.

more comprehensive understanding of uncertainty in TLS data, making it a valuable tool for applications that demand precise quantification of both random noise and systematic errors, such as deformation monitoring. Future work will focus on applying the method to real data, combining error ellipses and zonotopes to demonstrate the uncertainty budget of a point in relation to an object, as well as derive interval-based deformation analysis concepts.

Acknowledgements

This research received funding from the German Research Foundation (DFG) within the framework of Research Unit FOR 5455: Deformation Analysis Using Terrestrial Laser Scanner Measurements (TLS-Defo).

References

BIPM, IEC, IFCC, ILAC, ISO, IUPAC, IUPAP, OIML, n.d. Guide to the expression of uncertainty in measurement — Part 1: Introduction. Joint Committee for Guides in Metrology, JCGM GUM-1:2023.

Brunner, F., 1984. Modelling of atmospheric effects on terrestrial geodetic measurements. *Geodetic Refraction: Effects of electromagnetic Wave Propagation Through the Atmosphere*, Springer, 143–162.

Dbouk, H., 2021. Alternative Integrity Measures Based on Interval Analysis and Set Theory. PhD thesis, Fachrichtung Geodäsie und Geoinformatik der Leibniz Universität Hannover.

Ehambram, A., Voges, R., Brenner, C., Wagner, B., 2022. Interval-based visual-inertial lidar slam with anchoring poses. *2022 International Conference on Robotics and Automation (ICRA)*, IEEE, 7589–7596.

Greisinger Electronic GmbH, 2013. GFTB 200: Data Sheet.

Guyonneau, R., Lagrange, S., Hardouin, L., Lucidarme, P., 2014. Guaranteed interval analysis localization for mobile robots. *Advanced Robotics*, 28(16), 1067–1077.

Hennes, M., 2006. Das Nivelliersystem-Feldprüfverfahren nach ISO 17123-2 im Kontext refraktiver Störeinflüsse. *AVN*, 3(2006), 85–94.

Herzberger, G. A. J., Alefeld, J., 1983. Introduction to interval computations. *translated by J. Rokne, Academoic Press, New York, New York*.

Jaulin, L., Kieffer, M., Didrit, O., Walter, E., 2001. *Applied Interval Analysis with Examples in Parameter and State Estimation, Robust Control and Robotics*.

Kharaghani, G., 1987. Propagation of refraction errors in trigonometric height traversing and geodetic levelling. Technical report№ 132. University of New Brunswick.

Kutterer, H., 1994. *Intervallmathematische Behandlung endlicher Unschärfen linearer Ausgleichungsmodelle*. Beck.

Kutterer, H., 1999. On the sensitivity of the results of least-squares adjustments concerning the stochastic model. *Journal of Geodesy*, 73, 350–361.

Le Bars, F., Sanchez, R., Jaulin, L., Rohou, S., Rauh, A., 2022. An online interval-based inertial navigation system for control purposes of autonomous boats. *Frontiers in Control Engineering*, 2, 786188.

Leica GmbH, 2017. Leica ScanStation P50: Data Sheet.

Medić, T., Kuhlmann, H., Holst, C., 2019. Designing and evaluating a user-oriented calibration field for the target-based self-calibration of panoramic terrestrial laser scanners. *Remote Sensing*, 12(1), 15.

Möller, B., Beer, M., 2013. *Fuzzy randomness: uncertainty in civil engineering and computational mechanics*. Springer Science & Business Media.

Moore, R. E., Kearfott, R. B., Cloud, M. J., 2009. *Introduction to interval analysis*. SIAM.

Muralikrishnan, B., Ferrucci, M., Sawyer, D., Gerner, G., Lee, V., Blackburn, C., Phillips, S., Petrov, P., Yakovlev, Y., Astrelin, A. et al., 2015. Volumetric performance evaluation of a laser scanner based on geometric error model. *Precision Engineering*, 40, 139–150.

Reinhart, E., 1975. Exakte abschätzung von maximalfehlern aus vorgegebenen toleranzen der beobachtungsgrößen. Technical report, Institut für Astronomische und Physikalische Geodäsie.

Rüeger, J. M., 2012. *Electronic distance measurement: An introduction*. Springer Science & Business Media.

Schmitt, G., 1977. Some Considerations Using Interval Analysis in Adjustment Calculations. *Weitere Beiträge der Bundesrepublik Deutschland zur Vorlage hei der XVI Generalversammlung der IUGG, Grenoble 1975*, 87–97.

Schön, S., 2003. Analyse und Optimierung geodätischer Messanordnungen unter besonderer Beräcksichtigung des Intervallansatzes. PhD thesis.

Schön, S., Kutterer, H., 2005a. Realistic uncertainty measures for gps observations. *A Window on the Future of Geodesy: Proceedings of the International Association of Geodesy IAG General Assembly Sapporo, Japan June 30–July 11, 2003*, Springer, 54–59.

Schön, S., Kutterer, H., 2005b. Using zonotopes for overestimation-free interval least-squares–some geodetic applications. *Reliable Computing*, 11(2), 137–155.

Schön, S., Kutterer, H., 2006. Uncertainty in GPS networks due to remaining systematic errors: the interval approach. *Journal of Geodesy*, 80, 150–162.

Shen, N., Wang, B., Ma, H., Zhao, X., Zhou, Y., Zhang, Z., Xu, J., 2023. A review of terrestrial laser scanning (TLS)-based technologies for deformation monitoring in engineering. *Measurement*, 113684.

Soudarissanane, S., Lindenbergh, R., Menenti, M., Teunissen, P., 2011. Scanning geometry: Influencing factor on the quality of terrestrial laser scanning points. *ISPRS journal of photogrammetry and remote sensing*, 66(4), 389–399.

Su, J., Schön, S., 2021. Improved observation interval bounding for multi-gnss integrity monitoring in urban navigation. *Proceedings of the 34th International Technical Meeting of the Satellite Division of The Institute of Navigation (ION GNSS+ 2021)*, 4141–4156.

Su, J., Schön, S., 2022. Bounding the residual tropospheric error by interval analysis. *Geodesy for a Sustainable Earth: Proceedings of the 2021 Scientific Assembly of the International Association of Geodesy, Beijing, China, June 28–July 2, 2021*, Springer, 367–376.

Voges, R., Wagner, B., 2021. Interval-based visual-LiDAR sensor fusion. *IEEE Robotics and Automation Letters*, 6(2), 1304–1311.

Ziegler, G. M., 1995. Lectures on Polytopes, volume 152 of. *Graduate Texts in Mathematics*, 6–2.